PCCP

PAPER

View Article Online
View Journal





Cite this: DOI: 10.1039/c9cp02085c

# Molecular diffusion and nano-mechanical properties of multi-phase supported lipid bilayers

Tatsuhiro Maekawa,†[a] Hokyun Chin,†[b] Takashi Nyu,[a] Tun Naw Sut,[b] Abdul Rahim Ferhan,[b] Tomohiro Hayashi *[ac] and Nam-Joon Cho *[bd]

Understanding the properties of cell membranes is important in the fields of fundamental and applied biology. While the characterization of simplified biological membrane mimics comprising liquid phase lipids has been routinely performed due to the ease of fabrication, the characterization of more realistic membrane mimics comprising multi-phase lipids remains challenging due to more complicated fabrication requirements. Herein, we report a convenient approach to fabricate and characterize multi-phase supported lipid bilayers (SLBs). We employed the solvent-assisted lipid bilayer (SALB) formation method to fabricate mixed lipid bilayers comprising liquid phase 1,2-dioleoyl-*sn*-glycero-3-phosphocholine (DOPC) and gel phase 1,2-dipalmitoyl-*sn*-glycero-3-phosphocholine (DPPC) lipids at room temperature. The fabrication procedure was performed inside a newly designed microfluidic chamber, which facilitated the subsequent characterization of the SLBs without exposure to air. The SLBs were then characterized *via* fluorescence microscopy, fluorescence recovery after photobleaching (FRAP), atomic force microscopy (AFM) and AFM-based force-distance measurements. Interestingly, results from these characterization techniques revealed that regardless of the gel phase composition, the SALB formation method consistently yielded uniform SLBs at room temperature, even though the transition temperature of DPPC is considerably higher. Furthermore, the composition ratio of DOPC and DPPC in the precursor solution is well reproduced in the fabricated SLBs. We also identified from diffusivity measurements that a high ratio of gel phase lipid revitalizes lipid–lipid interactions, which led to reduced molecular fluidity and the suppression of thermal undulation within the SLBs. Taken together, our results highlight the robustness of the SALB formation method that allows the fabrication of complex lipid bilayers with a high degree of precision, which is suitable for functional studies of biological membranes.

Received 13th April 2019,
Accepted 5th July 2019

DOI: 10.1039/c9cp02085c

rsc.li/pccp

## Introduction

The importance of understanding the properties of cell membranes in various fields of fundamental and applied biology has motivated the development of complex model membranes that can accurately mimic the structure of biological membranes in their native form.[1–4] In order to investigate a complex model membrane, it is necessary to fabricate supported lipid bilayers (SLBs) comprising various lipid compositions, which may exist in different phases, including the gel phase.[5] Numerous strategies have been developed to prepare SLBs including Langmuir-type deposition,[6,7] bubble-collapse deposition,[8,9] dip-pen nanolithography,[10,11] spin coating,[12,13] lipid wetting[14,15] and vesicle fusion.[16,17] Vesicle fusion, which involves the adsorption and spontaneous rupture of precursor phospholipid vesicles on a solid support, represents one of the most popular approaches due to its simplicity.[16–20] However, when the vesicles contain phospholipids in the gel phase, which has a comparatively high transition temperature (*i.e.*, above room temperature), the large bending rigidities of the gel phase phospholipids hinder the rupture process when vesicle fusion is attempted at room temperature, preventing the formation of uniform SLBs.[21,22] Several works have circumvented this problem by raising the temperature (*i.e.*, above the transition temperature of the gel phase lipid) during the adsorption and vesicle rupture stages of the process and cooling the system down to room temperature only after the SLB has been completely formed.[23–25] Although these steps are rather straightforward within the context of SLB fabrication *per se*, the

[a] *Department of Materials Science and Engineering, School of Materials Chemical Technology, Tokyo Institute of Technology, 4259 Nagatsuta-cho, Midori-ku, Yokohama, Kanagawa 226-8503, Japan. E-mail: hayashi@echem.titech.ac.jp*
[b] *School of Materials Science and Engineering, Nanyang Technological University, 50 Nanyang Drive, 637553, Singapore. E-mail: NJCho@edu.ntu.sg*
[c] *JST-PRESTO, 4-1-8 Hon-cho, Kawaguchi-shi, Saitama 332-0012, Japan*
[d] *School of Chemical and Biomedical Engineering, Nanyang Technological University, 62 Nanyang Drive, 637459, Singapore*
† Equally contributed as co-first authors.

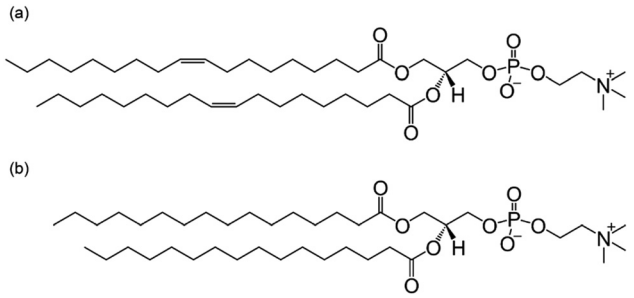


Fig. 1 Chemical structures of (a) DOPC and (b) DPPC.

temperature changes greatly complicate SLB characterization using surface-based techniques that are sensitive to the bulk environment due to large thermal fluctuations that make it difficult to extract reliable kinetic information.

To overcome the aforementioned limitation, a solvent-assisted lipid bilayer (SALB) formation method has been developed to fabricate SLBs on a support substrate in a flow channel following a solvent exchange process from organic solvents (*e.g.*, isopropanol, methanol, and ethanol) to aqueous solvents (*e.g.*, water and buffer).[21,26–29] In organic solvents, the lipid molecules exist as monomers or form reverse micelles. During the solvent exchange step, the concentration of the organic solvent in the flow channel gradually decreases, leading to the transition of lipid molecules to form normal micelles and vesicles.[30,31] This ultimately leads to the formation of SLB on the support substrate, when the solvent in the flow channel has been fully exchanged to the aqueous solution.[31] Most notably, the SALB method can form SLBs with complex components and comprising gel phase phospholipids at room temperature without requiring vesicles.[29,32]

The establishment of the SALB method, therefore, spurred us to investigate more complex SLBs comprising lipids in different phases. To achieve this, it is imperative to utilize a fluidic chamber that enables the solvent exchange step to be performed with precise control over the solution flow rate and with a perfect sealing environment at the micron level. At the same time, the dimensions of the chamber should allow optical access of microscopes and enable an atomic force microscope (AFM) tip to approach the SLBs. Commercially available liquid chambers or open-ended Petri dish systems do not satisfy all of the above conditions and introduce several drawbacks such as the ease of forming defects by means of generating air bubbles on the bilayer surface due to the lack of proper sealing.[16,23,33] To address this issue, we design a microfluidic chamber that can be integrated with a commercial optical microscope (Eclipse TE 2000, Nikon) and an AFM (Asylum Research MFP-3D-BIO, Oxford Instruments, USA) system. Conceptually, the novelty of our AFM-compatible microfluidic chamber lies in the ability to precisely control the flow rate inside the flow channel without hindering operations of the optical microscope and AFM setup.[33] In addition, the robust microfluidic chamber permits multiple solvent exchange steps without solvent leakage in a liquid environment.

In order to confirm the feasibility of forming multi-phase SLBs inside the microfluidic chamber, we fabricate SLBs comprising liquid phase 1,2-dioleoyl-*sn-glycero*-3-phosphocholine (DOPC, transition temperature = −17 °C) and gel phase 1,2-dipalmitoyl-*sn-glycero*-3-phosphocholine (DPPC, transition temperature = 41 °C) (Fig. 1). To this end, the formation of SLBs comprising DOPC and DPPC under ambient conditions has been challenging using the vesicle fusion method since the transition temperature of DPPC is higher than room temperature.[34,35] In order to form SLBs with a relatively high fraction of DPPC, the experiment would have to be performed above the transition temperature. As mentioned earlier, this would hamper effective characterization of the SLB since the high temperature would affect the signal-to-noise ratio in most analytical tools, including AFM. Herein, we employ the SALB formation method to fabricate multi-phase DOPC–DPPC SLBs in our newly designed microfluidic chamber. We then perform a series of downstream characterization steps on the SLBs including fluorescence microscopy imaging, fluorescence recovery after photobleaching (FRAP), AFM visualization and AFM-based force–distance measurements to compare the biophysical properties of pure liquid phase SLBs and multi-phase SLBs, and investigate the effect of increasing the gel phase composition on the biophysical property of the SLB.

Table 1 Composition ratios of the lipid mixtures used in the fabrication of SLBs by the SALB method

| DOPC (mol%) | DPPC (mol%) | Rhodamine-PE (mol%) |
|---|---|---|
| 100 | 0 | 0.7 |
| 80 | 20 | 0.7 |
| 60 | 40 | 0.7 |
| 40 | 60 | 0.7 |
| 20 | 80 | 0.7 |

## Materials and methods

### Lipid solution preparation

DOPC, DPPC, and 1,2-dioleoyl-*sn-glycero*-3-phosphoethanolamine-*N*-(lissamine rhodamine B sulfonyl) (ammonium salt) (Rhod PE) were purchased from Avanti Polar Lipids (Alabaster, AL, USA). Chloroform solutions of DOPC, DPPC, and Rhod PE were mixed in glass vials to prepare lipid solutions at different composition ratios. The composition ratios of the lipid mixtures are summarized in Table 1. The solution mixtures were then dried with a nitrogen gas stream, and the dried lipid films were placed in a vacuum chamber overnight. The dried lipid films were rehydrated in 2 mL isopropanol (Fujifilm Wako Pure Chemical Corporation, Japan) to obtain a lipid concentration of 0.5 mg $mL^{-1}$.

### Microfluidic chamber design

To observe the lipid bilayer under a fluorescence microscope and seamlessly perform AFM measurements post-fabrication without exposure to air, we designed a microfluidic chamber device wherein SLBs can be fabricated *via* the SALB technique (Fig. 2). All experiments were conducted using the new microfluidic chamber, which has a rectangular flow channel measuring 26 mm in length, 6 mm in width, and 0.5 mm in height.

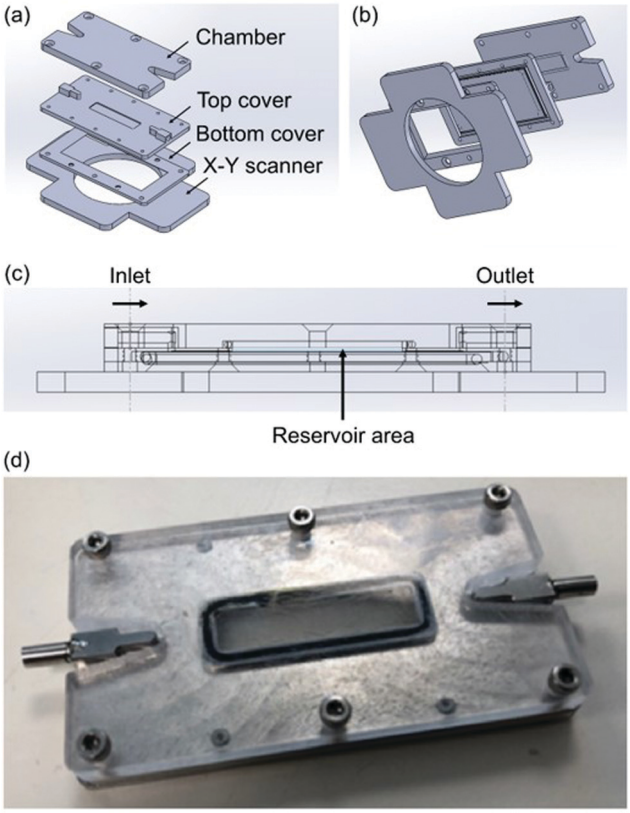


Fig. 2 (a) Three-dimensional drawing of the different parts of the microfluidic chamber. (b) Reverse (bottom-up) perspective of the three-dimensional drawing. (c) Cross-sectional view of the microfluidic channel area. (d) Photograph of the assembled microfluidic chamber for MFP-3D AFM.

The entire chamber consists of six components. The top cover of the chamber is tightly fixed to the flow channel section with six bolts to prevent the solvent leakage. Two rubber O-rings of different sizes absorb the pressure to the coverslip (22 mm × 50 mm) from the bottom cover, acting as a sealant for the chamber. There are inlet and outlet ports leading into and out of the flow channel for insertion of tubes. Overall, the chamber measures 62 mm in length and 33 mm in width and can be easily mounted and magnetically fixed onto an AFM stage.

### Supported lipid bilayer fabrication

A coverslip (22 mm × 50 mm) (Fisher Scientific, USA) was ultrasonically cleaned for 20 min in DI water, followed by drying under a stream of nitrogen gas. The active surface of the coverslip (*i.e.*, where the SLB is fabricated on) was made hydrophilic by treating it with an oxygen plasma glow discharge using a hydrophilizing treatment device (HDT-400, JEOL Datum, Tokyo, Japan) for 1 min immediately before use. The microfluidic chamber was assembled with the inlet and outlet tubes and the coverslip. Tris buffer (10 mM Tris (Wako, Japan), 150 mM NaCl (Wako, Japan), and pH 7.5) was first injected into the microfluidic chamber at a flow rate of 200 μL $min^{-1}$ using a peristaltic pump (Ismatec Reglo Digital ISM 833, Germany). After that, Tris buffer was replaced by introducing isopropanol at the same flow rate, and phospholipids dissolved in isopropanol (4 mL) were injected into the microfluidic chamber at a flow rate of 100 μL $min^{-1}$ for 25 min. Finally, the solvent exchange step was performed by injecting Tris buffer into the chamber at a flow rate of 50 μL $min^{-1}$ for 30 min, resulting in the formation of SLB on the coverslip.

### Epifluorescence microscopy and fluorescence recovery after photobleaching

An inverted epifluorescence Eclipse TE 2000 microscope (Nikon) equipped with a 60× oil immersion objective (numerical aperture, NA = 1.49) and an Andor iXon+ EMCCD camera (Andor Technology, Belfast, Northern Ireland) was employed to observe the lipid film with Rhod PE after SLB formation is completed. All fluorescence micrographs were acquired from at least three different areas per sample. The resolution was 512 × 512 pixels with a scan area of 136 × 136 $\mu m^2$. The samples were illuminated through a TRITC filter set by a mercury lamp (Intensilight C-HGFIE, Nikon, Tokyo, Japan). The fluorescence intensities of the micrographs were computed using the ImageJ software. Fluorescence recovery after photobleaching (FRAP) measurements were performed on the same platform. A laser beam (532 nm, 100 mW) was irradiated onto the SLB for 5 seconds, resulting in the photobleaching of a circular region ∼35 μm in diameter. The recovery of fluorescence intensity in the bleached region was recorded at every two-second interval over a total duration of 3 minutes. The diffusivities of the SLBs were calculated in MATLAB using a Hankel transform method.[36]

### Atomic force microscopy

A commercial atomic force microscope system (Asylum Research MFP-3D-BIO, Oxford Instruments, USA) was employed to perform the AFM height scan and force spectroscopy experiments. A single-crystal silicon cantilever (NSG03, NT-MDT, Moscow, Russia), with a nominal tip curvature of 6 nm in radius and a resonance frequency of about 90 kHz in air, and 30–50 kHz in aqueous buffer, was utilized for all experiments. The nominal spring constant was 2.0 N $m^{-1}$, which was calibrated by measuring the thermal noise.[37] All height scans were obtained in Tris buffer at room temperature (25 °C). The scans were conducted in contact mode over an area of 10 × 10 $\mu m^2$ and a scan rate of around 0.3–0.5 Hz was used to reduce the possibility of damaging the multi-phase SLBs during the scan and minimize the signal noise. All force measurements were performed in Tris buffer at room temperature (25 °C), and force maps were recorded in contact mode. The trace and retrace speeds of the cantilever were fixed at 4 mm $s^{-1}$, and a maximum loading force of 30 nN was applied. The resolution was set to 100 × 100 points with a scan area of 10 × 10 $\mu m^2$, generating 10 000 force curves for every single run of force mapping (100 × 100 $nm^2$ per point). To translate the deflection signal of the cantilever to the tip-surface separation, we defined the separation of zero at the point where linearity in the constant compliance region began in the force–displacement curve.[38] To analyze the sample thickness, we defined the point where the cantilever received a

repulsive force as the bilayer-probe contact point at which the value of the force increased by three consecutive points and taking a value of force larger than a force detected by thermal fluctuation. The force curves were processed using the Igor Pro software.

## Results and discussion

### Fluorescence microscopy and diffusion coefficient measurement analysis

Fluorescence microscopy images taken from SLBs comprising different ratios of DOPC and DPPC lipids are shown in Fig. 3a–e. Since the DOPC lipids are dye-labeled, the fully liquid phase SLB comprising only DOPC exhibits uniform fluorescence intensity over the scanned surface (Fig. 3a). In the presence of gel phase DPPC lipids, which are unlabelled, distinct regions of lower fluorescence intensity (dark domains) start to become observable (Fig. 3b). As the fraction of DPPC increases, the dark domains grow in coverage (Fig. 3c–e).[39,40] The appearance of dark regions that become more apparent with increasing amount of rigid phase constituent is consistent with our previous works where cholesterol-containing SLBs also demonstrate similar behaviors with increasing fraction of cholesterol.[21,22] However, in this case, it is interesting to note that when the DPPC fraction was increased up to 40 mol%, the dark domains significantly grow in size while maintaining their spatial distribution (Fig. 3c). Upon further increase in DPPC fraction from 40 mol% to 60 mol%, the dark domains become dispersed into smaller circular regions that are rather homogenous in size and are uniformly spread over the scanned surface (Fig. 3d). At the highest tested DPPC fraction of 80 mol%, the dark regions become merged, sprawling across the surface, resulting in a dramatic increase in lateral coverage (Fig. 3e).

We proceeded to check the composition of lipids in the SLB based on the average fluorescence intensities. Since the SLBs comprise dye-labeled DOPC and unlabelled DPPC lipids, the fluorescence intensity will be directly correlated to the fraction of DOPC lipid. Specifically, the maximum fluorescence intensity will be observed for SLB comprising 100 mol% DOPC lipid and zero fluorescence intensity will be observed for SLB comprising zero mole percent DOPC lipid (*i.e.*, 100 mol% DPPC lipid).

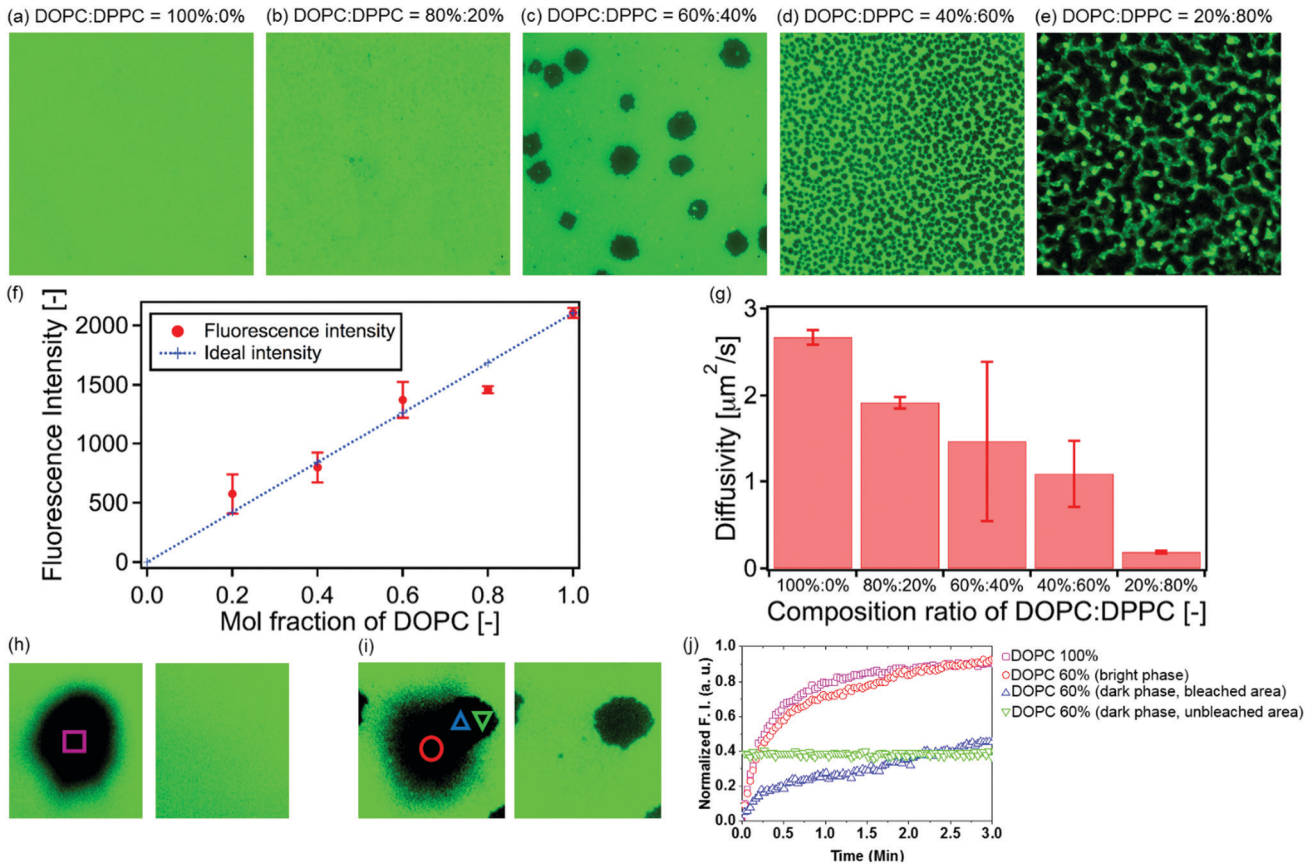


Fig. 3 Fluorescence micrographs of the SLBs fabricated following the SALB formation method. The DOPC : DPPC lipid composition ratios of the SLBs shown in the micrographs are (a) 100 : 0 mol%, (b) 80 : 20 mol%, (c) 60 : 40 mol%, (d) 40 : 60 mol%, and (e) 20 : 80 mol%, each containing 0.7 mol% fluorescent Rhod PE dye lipid. Each micrograph measures 136 × 136 μm$^2$. (f) Fluorescence intensities at different DOPC mole fractions in the precursor mixtures. (g) Molecular diffusivities evaluated by FRAP measurements. In (f) and (g), the error bars represent standard deviation ($n$ = 5). Fluorescence micrographs immediately after photobleaching (left) and after a 3 min recovery period (right) of SLBs comprising (h) 100% DOPC and (i) DOPC : DPPC = 60 : 40 mol%. (j) Recovery curves corresponding to the bright and dark areas. Each symbol corresponds to the respective annotated area in (h) and (i).

Conversely, in a plot of fluorescence intensity against DOPC mole fraction (Fig. 3f), the straight line connecting the origin to the experimentally determined maximum intensity originating from SLB comprising 100 mol% DOPC lipid (*i.e.*, 2000 intensity a.u.) serves as a reference to obtain the expected fluorescence intensity for a certain DOPC mole fraction in the SLB. Hence, by comparing the actual fluorescence intensity obtained using a certain DOPC mole fraction in the precursor lipid mixture to the expected fluorescence intensity in the formed SLB based on this linear correlation, we can determine the degree of compositional reproducibility during the SLB formation process. In particular, if the observed fluorescence intensity lies on the straight line, the DOPC mole fraction in the formed SLB perfectly matches the DOPC mole fraction in the precursor lipid mixture. If the observed fluorescence intensity lies below the straight line, the DOPC mole fraction in the formed SLB is lower than expected (*i.e.*, lower than the DOPC mole fraction in the precursor lipid mixture), and *vice versa*. Based on this, we deduce from the plot in Fig. 3f that the experimentally determined fluorescence intensities all lie close to the 'ideal intensity' line, supporting that the composition of lipids in the precursor solution mixture is well reproduced on the substrate when the SLB is fabricated following the SALB formation method. It is worthy to note that the slight mismatch between the ratio of dark and bright regions to the lipid fraction can be attributed to the lack of spatial resolution of the optical microscope (*i.e.*, around 500 nm in lateral dimension), which is not sufficient to observe domains with dimensions in the 100 nm range.

We then proceeded to measure the membrane diffusivities of the SLBs comprising different DOPC/DPPC compositions to (1) evaluate the diffusivity of SLBs obtained *via* the SALB formation method in comparison to SLBs obtained *via* vesicle fusion and more importantly (2) investigate the effect of increasing gel phase on the overall membrane diffusivity. We calculated the diffusivities of the SLBs using the Hankel transform method, and the calculations were implemented in MATLAB. In brief, the Hankel transform method employs circular averaging of the analyzed data (in this case the fluorescence intensity of the photobleached area of the SLB) to obtain a mathematical curve fitting of the fluorescence recovery profile before the diffusivity value is extracted from the fitted curve.[36] Our calculations revealed a gradual decrease in the overall diffusivity of the membrane with an increasing fraction of DPPC (Fig. 3g), in agreement with previous observations.[41,42] For fully liquid phase SLBs comprising 100% DOPC lipids, the calculated diffusivity was 2.6 ± 0.1, which agrees well with previously reported values.[26,43,44] Conversely, this further testifies that SLBs fabricated following the SALB formation method possess the same physicochemical properties (*i.e.*, molecular density and diffusivity) as SLBs prepared *via* the vesicle fusion method.

The high mobility of the lipid molecules in the film is one of the characteristics of liquid phase SLBs, which is difficult to observe for unordered aggregated or randomly adsorbed lipid molecules.[45,46] Hence, to understand the effect of increasing gel phase fraction on the reduced overall membrane diffusivity, it is imperative first to prove that the dark domains are indeed regions of lipid bilayers in the rigid phase. The lipids in this region should still possess some degree of mobility, albeit considerably reduced. Following this line, we show representative sets of raw fluorescence micrographs from photobleached SLBs comprising 100% DOPC (Fig. 3h) and photobleached SLBs comprising 60% DOPC and 40% DPPC (Fig. 3i), before and after fluorescence recovery. In the case of the latter, the photobleached area included a large dye-labeled region and a small portion of the dark region. Based on the fluorescence recovery profiles taken from the different regions (Fig. 3j), our results

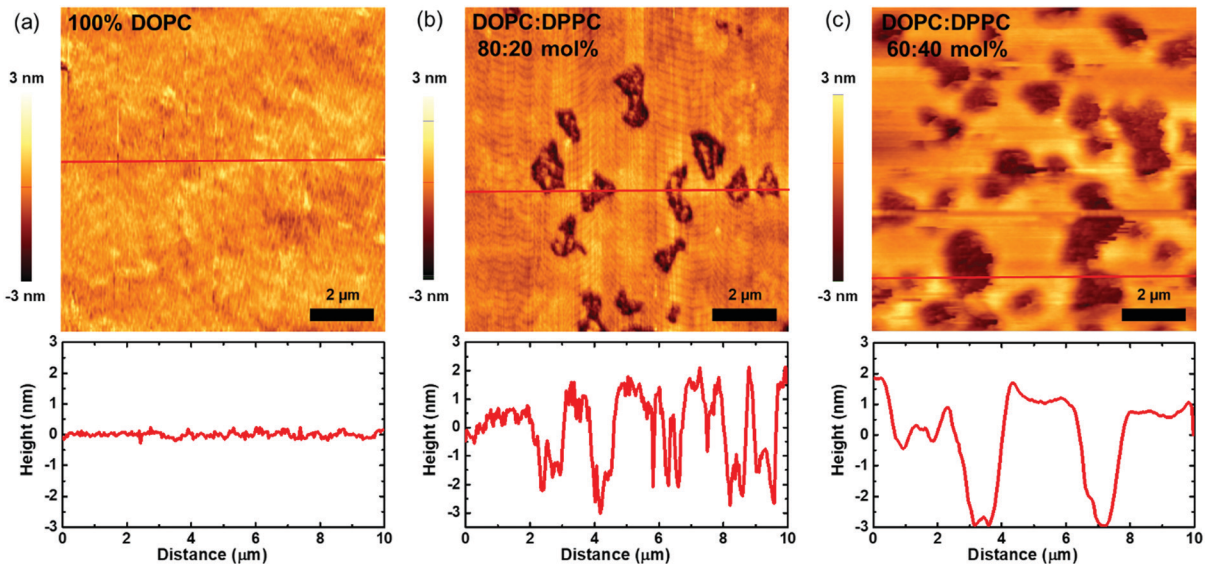


Fig. 4 Comparison of AFM height retraces and their corresponding cross-sectional height profiles across the surface, denoted by the red line, obtained from SLBs with different DOPC : DPPC compositions. The DOPC : DPPC lipid composition ratios of the SLBs shown in the height retraces are (a) 100 : 0 mol%, (b) 80 : 20 mol%, and (c) 60 : 40 mol%.

clearly show a recovery of fluorescence intensity in the area of mixed bilayer after the photobleaching, indicating that the lipid molecules freely diffuse within the film, which is an important characteristic of SLBs. It is worthy to note that this is also a testimony that a complete SLB has been formed and the dark regions are not bilayer defects or "holes". However, while the diffusivity of the dye-labeled region did not differ significantly between the two SLBs, the diffusivity of the dark region (*i.e.*, which is bleached) in the SLB comprising 60% DOPC and 40% DPPC was significantly lower. We attribute the differences in diffusivities to the fact that DPPC possesses two palmitic acid groups with a linear carbon chain. As such, they are packed at high density in the bilayer due to attractive van der Waals interaction between the chains. On the other hand, the chains of DOPC include carbon double bonds, which lead to steric hindrance that deters them from packing densely. Therefore, the observed overall diffusivity of the SLB is lower when it contains higher fractions of DPPC.

### Nano-mechanical properties of multi-phase supported lipid bilayers evaluated by AFM

To evaluate the morphological and nano-mechanical properties of the multi-phase lipid bilayer in detail, we conducted a set of quantitative nano-mechanical analyses by AFM using the originally designed microfluidic chamber. We first performed a conventional raster scan to observe the surface morphology of the SLBs. As expected, slight differences in surface morphology were observed for SLBs comprising different ratios of DOPC and DPPC. For a pure DOPC SLB, a smooth surface with height variations of less than 0.5 nm was observed (Fig. 4a), which verifies the uniformity of the bilayer. In the presence of DPPC, phase domains were clearly visible, confirming the successful formation of a liquid–gel phase mixture. For the SLB comprising 80 mol% DOPC and 20 mol% DPPC, isolated domains with lateral dimensions in the range of 1 μm were observed (Fig. 4b). The height variations across the scanned surface were in the range of 3–4 nm. In comparison, for the SLB comprising 60 mol% DOPC and 40 mol% DPPC, slightly larger domains were observed with greater lateral coverage (Fig. 4c). The height variations across the scanned surface were in the range of 4–5 nm. Taken together, the overall trend observed through the AFM height scans agrees well with observations from fluorescence microscopy. We then conducted penetration force measurements on the SLBs to evaluate changes in bilayer rigidity using the AFM probe tip.

With reference to the force–distance (*f*–*d*) curve, the penetration force is defined as the amount of force required to disrupt the bilayer after the first point of contact by the AFM tip (Fig. 5a). In brief, when the tip comes into contact with the bilayer with typical separation depth of 5 to 10 nm, a repulsive force arises.[47,48] Upon further approach of the tip towards the substrate, the repulsive force increases as a result of bilayer compression. After compression of the bilayer, the film collapses at a separation of 2 to 3 nm, which leads to the tip jumping into hard contact with the underlying substrate.[49] The penetration depth is therefore defined as the distance between these two points – one is the point at which the repulsive force begins to rise after the initial contact between the tip and the bilayer, and the other is the point at which hard contact occurs between the tip and substrate.[50–52] Supported lipid bilayers are known to be formed on a hydration layer with a thickness of about 1 nm.[51,53] As such, the penetration depth evaluated from the *f*–*d* curves is the sum of the thicknesses of the hydration layer and the bilayer, which is typically around 4–5 nm.[54–56] Representative force–distance curves obtained from SLBs clearly show differences in penetration force and penetration distance for SLBs with different DOPC/DPPC compositions (Fig. 5b),

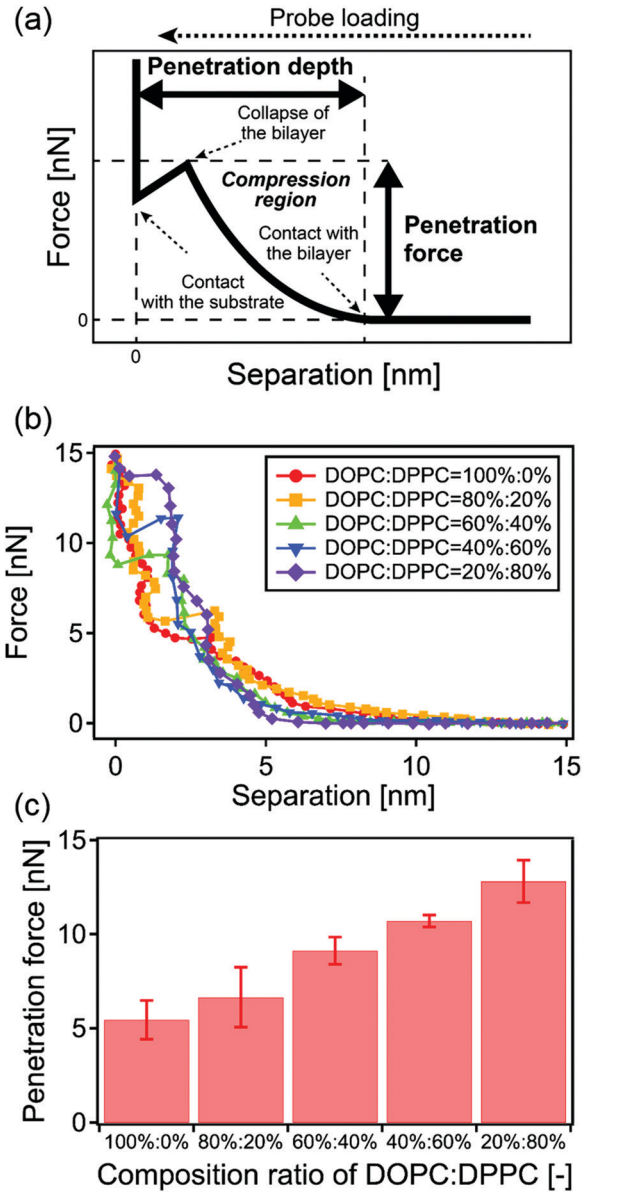


Fig. 5 (a) Definitions of penetration depth and penetration force in this work. (b) Representative force-separation curves recorded from SLBs fabricated following the SALB formation method in Tris buffer solution. (c) Average values of the penetration force observed from SLBs containing different ratios of DOPC and DPPC. Error bars represent standard deviation ($n$ = 5).

which is in the range of 5–7 nm, in close agreement with previous works.

The plot of calculated averaged penetration force against compositional ratio shows a direct relationship between these two parameters (Fig. 5c). With an increasing fraction of gel phase DPPC, the penetration force is higher, indicating that DPPC increases the rigidity of the bilayer. The increase in the rigidity at high fractions of DPPC can be explained by the intermolecular interactions that are strengthened by the presence of DPPC.[35,39] At higher fractions of DPPC, the penetration depth of the bilayers is smaller compared to that of the pure DOPC bilayer. As earlier discussed, the results from FRAP and force spectroscopy measurements suggest that the bilayer rigidity is higher and the diffusivity of the molecules in the bilayer decreases because of the strong intermolecular interactions between the DOPC and DPPC lipid molecules. As a consequence, the thermal undulation also decreases, resulting in lower penetration depths.

## Conclusion

We fabricated SLBs comprising both liquid phase DOPC and gel phase DPPC at different composition ratios following the SALB formation method inside a newly developed microfluidic chamber at room temperature. This enabled us to seamlessly perform a series of physical characterizations on the SLBs without exposure to air. Our multi-pronged analysis using the fluorescence microscope and AFM testified the ability of the SALB method to form uniform multi-phase SLBs even when they comprise a significantly high fraction of gel phase lipids (*i.e.*, up to 80 mol% DPPC), which is challenging using the conventional vesicle fusion method. The composition of lipids in the precursor solution was well reproduced on the substrate, indicating that the SALB formation method allows the precise control of the lipid composition in the fabricated SLBs. Using the SLBs that have been obtained with precise control over its composition (*i.e.*, from zero up to 80 mol% DPPC, at 20 mol% intervals), we investigated the effect of increasing gel phase fraction on the biophysical properties of the SLBs. We found that with increasing fraction of DPPC, the overall diffusivity of lipid molecules in the SLBs decreases and the rigidity of the films increases. This observation was attributed to differences in molecular structure, which governs the molecular organization and influences intermolecular interactions between liquid phase and gel phase lipid molecules. Taken together, the results in this work demonstrate that the SALB formation method represents a promising approach to fabricate high-quality complex multi-phase model membranes that mimic biological membranes of living systems. More importantly, it paves the way for more detailed qualitative and quantitative investigations on such biological mimics.

## Conflicts of interest

The authors declare no conflicts of interest.

## Acknowledgements

This work was supported by the National Research Foundation of Singapore through a Competitive Research Programme grant (NRF-CRP10-2012-07) and a Proof-of-Concept grant (NRF2015NRF-POC0001-19) as well as through the Center for Precision Biology at Nanyang Technological University. The author (Tomohiro Hayashi) acknowledges the financial supports by KAKENHI (19H02565, 17K20095 and 15KK0184) and JST-PRESTO. The authors appreciate the help of Ms Kazue Taki for the administration of this project.

## References

1 E.-K. Sinner and W. Knoll, *Curr. Opin. Chem. Biol.*, 2001, **5**, 705–711.
2 E. Sackmann, *Science*, 1996, **271**, 43–48.
3 Y.-H. M. Chan and S. G. Boxer, *Curr. Opin. Chem. Biol.*, 2007, **11**, 581–587.
4 G. J. Hardy, R. Nayak and S. Zauscher, *Curr. Opin. Colloid Interface Sci.*, 2013, **18**, 448–458.
5 H. A. Rinia and B. de Kruijff, *FEBS Lett.*, 2001, **504**, 194–199.
6 L. K. Tamm and H. M. McConnell, *Biophys. J.*, 1985, **47**, 105–113.
7 A. P. Girard-Egrot and L. J. Blum, in *Nanobiotechnology of Biomimetic Membranes*, ed. D. K. Martin, Springer US, Boston, MA, 2007, pp. 23–74, DOI: 10.1007/0-387-37740-9_2.
8 M. D. Mager, B. Almquist and N. A. Melosh, *Langmuir*, 2008, **24**, 12734–12737.
9 M. D. Mager and N. A. Melosh, *Langmuir*, 2007, **23**, 9369–9377.
10 M. Hirtz, A. Oikonomou, T. Georgiou, H. Fuchs and A. Vijayaraghavan, *Nat. Commun.*, 2013, **4**, 2591.
11 S. Lenhert, P. Sun, Y. Wang, H. Fuchs and C. A. Mirkin, *Small*, 2007, **3**, 71–75.
12 U. Mennicke and T. Salditt, *Langmuir*, 2002, **18**, 8172–8177.
13 A. Dols-Perez, L. Fumagalli, A. C. Simonsen and G. Gomila, *Langmuir*, 2011, **27**, 13165–13172.
14 J. Raedler, H. Strey and E. Sackmann, *Langmuir*, 1995, **11**, 4539–4548.
15 J. Nissen, S. Gritsch, G. Wiegand and J. O. Rädler, *Eur. Phys. J. B*, 1999, **10**, 335–344.
16 R. Richter, A. Mukhopadhyay and A. Brisson, *Biophys. J.*, 2003, **85**, 3035–3047.
17 R. P. Richter, R. Bérat and A. R. Brisson, *Langmuir*, 2006, **22**, 3497–3505.
18 J. A. Jackman, Z. Zhao, V. P. Zhdanov, C. W. Frank and N.-J. Cho, *Langmuir*, 2014, **30**, 2152–2160.
19 J. A. Jackman, J.-H. Choi, V. P. Zhdanov and N.-J. Cho, *Langmuir*, 2013, **29**, 11375–11384.
20 E. Kalb, S. Frey and L. K. Tamm, *Biochim. Biophys. Acta, Biomembr.*, 1992, **1103**, 307–316.
21 S. R. Tabaei, J. A. Jackman, S.-O. Kim, B. Liedberg, W. Knoll, A. N. Parikh and N.-J. Cho, *Langmuir*, 2014, **30**, 13345–13352.
22 S. R. Tabaei, J. A. Jackman, B. Liedberg, A. N. Parikh and N.-J. Cho, *J. Am. Chem. Soc.*, 2014, **136**, 16962–16965.
23 M.-P. Mingeot-Leclercq, M. Deleu, R. Brasseur and Y. F. Dufrêne, *Nat. Protoc.*, 2008, **3**, 1654.

24 T. K. Lind, M. Cárdenas and H. P. Wacklin, *Langmuir*, 2014, **30**, 7259–7263.
25 B. Seantier, C. Breffa, O. Félix and G. Decher, *Nano Lett.*, 2004, **4**, 5–10.
26 S. R. Tabaei, J.-H. Choi, G. Haw Zan, V. P. Zhdanov and N.-J. Cho, *Langmuir*, 2014, **30**, 10363–10373.
27 S. R. Tabaei, J. A. Jackman, S.-O. Kim, V. P. Zhdanov and N.-J. Cho, *Langmuir*, 2015, **31**, 3125–3134.
28 S. R. Tabaei, S. Vafaei and N.-J. Cho, *Phys. Chem. Chem. Phys.*, 2015, **17**, 11546–11552.
29 S. R. Tabaei, J. A. Jackman, M. Kim, S. Yorulmaz, S. Vafaei and N.-J. Cho, *J. Visualized Exp.*, 2015, **106**, e53073.
30 J. T. Buboltz and G. W. Feigenson, *Biochim. Biophys. Acta, Biomembr.*, 1999, **1417**, 232–245.
31 A. O. Hohner, M. P. C. David and J. O. Rädler, *Biointerphases*, 2010, **5**, 1–8.
32 J. J. Gillissen, S. R. Tabaei and N.-J. Cho, *Phys. Chem. Chem. Phys.*, 2016, **18**, 24157–24163.
33 H. Chin, J. J. Gillissen, E. Miyako and N.-J. Cho, *Rev. Sci. Instrum.*, 2019, **90**, 046105.
34 S. J. Attwood, Y. Choi and Z. Leonenko, *Int. J. Mol. Sci.*, 2013, **14**, 3514–3539.
35 Z. Leonenko, E. Finot, H. Ma, T. Dahms and D. Cramb, *Biophys. J.*, 2004, **86**, 3783–3793.
36 P. Jönsson, M. P. Jonsson, J. O. Tegenfeldt and F. Höök, *Biophys. J.*, 2008, **95**, 5334–5348.
37 J. L. Hutter and J. Bechhoefer, *Rev. Sci. Instrum.*, 1993, **64**, 1868–1873.
38 T. Hayashi, Y. Tanaka, Y. Koide, M. Tanaka and M. Hara, *Phys. Chem. Chem. Phys.*, 2012, **14**, 10196–10206.
39 P. Uppamoochikkal, S. Tristram-Nagle and J. F. Nagle, *Langmuir*, 2010, **26**, 17363–17368.
40 P. E. Milhiet, M. C. Giocondi, O. Baghdadi, F. Ronzon, C. Le Grimellec and B. Roux, *Single Mol.*, 2002, **3**, 135–140.
41 D. Scherfeld, N. Kahya and P. Schwille, *Biophys. J.*, 2003, **85**, 3758–3768.
42 J. Korlach, P. Schwille, W. W. Webb and G. W. Feigenson, *Proc. Natl. Acad. Sci. U. S. A.*, 1999, **96**, 8461.
43 S. Ladha, A. Mackie, L. Harvey, D. Clark, E. Lea, M. Brullemans and H. Duclohier, *Biophys. J.*, 1996, **71**, 1364–1373.
44 A. Åkesson, T. Lind, N. Ehrlich, D. Stamou, H. Wacklin and M. Cárdenas, *Soft Matter*, 2012, **8**, 5658–5665.
45 S. Garg, J. Rühe, K. Lüdtke, R. Jordan and C. A. Naumann, *Biophys. J.*, 2007, **92**, 1263–1270.
46 R. Tero, K. Fukumoto, T. Motegi, M. Yoshida, M. Niwano and A. Hirano-Iwata, *Sci. Rep.*, 2017, **7**, 17905.
47 H. Asakawa and T. Fukuma, *Nanotechnology*, 2009, **20**, 264008.
48 Y. F. Dufrêne, D. Martínez-Martín, I. Medalsy, D. Alsteens and D. J. Müller, *Nat. Methods*, 2013, **10**, 847–854.
49 S. Garcia-Manyes and F. Sanz, *Biochim. Biophys. Acta, Biomembr.*, 2010, **1798**, 741–749.
50 C. Das, K. H. Sheikh, P. D. Olmsted and S. D. Connell, *Phys. Rev. E: Stat., Nonlinear, Soft Matter Phys.*, 2010, **82**, 041920.
51 M. H. Abdulreda and V. T. Moy, *Biophys. J.*, 2007, **92**, 4369–4378.
52 V. Franz, S. Loi, H. Müller, E. Bamberg and H.-J. Butt, *Colloids Surf., B*, 2002, **23**, 191–200.
53 T. Fukuma, M. J. Higgins and S. P. Jarvis, *Biophys. J.*, 2007, **92**, 3603–3609.
54 C. Montis, S. Busatto, F. Valle, A. Zendrini, A. Salvatore, Y. Gerelli, D. Berti and P. Bergese, *Adv. Biosyst.*, 2018, **2**, 1700200.
55 N. Kučerka, S. Tristram-Nagle and J. F. Nagle, *J. Membr. Biol.*, 2006, **208**, 193–202.
56 E. Drolle, N. Kučerka, M. I. Hoopes, Y. Choi, J. Katsaras, M. Karttunen and Z. Leonenko, *Biochim. Biophys. Acta, Biomembr.*, 2013, **1828**, 2247–2254.

 